Sensors & Transducers, Vol. 236, Issue 8, August 2019, pp. 28-39

Sensors & Transducers

Published by IFSA Publishing, S. L., 2019
http://www.sensorsportal.com

3D-Cage Structured Biomimetic MMP-2/HSP60-Like Organo-Metallic Devices Sensitively Response to ATP Concentration Change Used for Defining the Anti-inflammatory and Pro-inflammatory Status

[1] E. T. CHEN, [2] J. T. THORNTON, [3] S.-H. DUH

[1] Advanced Biomimetic Sensors, Inc., 6710A Rockledge Drive, Suite 400, Bethesda, MD 20817, USA
[2] Bruker Nano, 19 Fortune Dr., Billerica, MA 01821, USA
[3] University of Maryland Medical System, 22 South Greene St, Baltimore, MD 21201, USA
Tel.: 240-706-5687, fax: 240-630-4051
[1] E-mail: ellenchen@nanobiomimeticsensors.com

Received: 18 June 2019 /Accepted: 22 July 2019 /Published: 31 August 2019

Abstract: ATP concentrations affecting the anti-inflammatory and the pro-inflammatory status were conducted based on directly testing ATP concentration in the biological samples using organo-metallic devices. A heat-damaged biomimetic Matrix Metalloproteinase-2 (MMP-2) / Heat Shock Protein (HSP 60) Sensor 1 as a "Stressful" model was tested in the presence of 60 nM ATP using organic milk samples, and significant ATP extracellular hydrolysis curves were observed compared with the human milk samples, that raised the superconductivity at zero-bias. The reversible membrane potential (RMP) change in the presence of ATP from 100 aM to 800 nM was tested using a "Healthy" 3D-cage biomimetic MMP-2/ HSP60-like device 2, the RPM maintained constant with 1.3 % voltage increase rate compared with that of the ATP. Results of two levels of LPS challenges on the two types of milk samples in the presence of 60 nM ATP using Sensor 2, show organic milk vulnerable with 18.8 ± 0.3 % recoveries at 90 fg/mL LPS compared 103 ± 0.7 % recovery for human milk samples.

Keywords: 3D-Cage Structure Membrane, Biomimetic MMP-2/HSP60 Multiple Functioning Device, ATP Quantitation, Biological Specimens, Reversible Membrane Potential (RMP), Ratio of Action/Resting potential.

1. Introduction

Literature reported ATP hydrolyzation extracellularly induces cancer cells drug resistance [1-4]. Assessing human milk immunological advantage over cow milk in preventing extracellular ATP hydrolyzation is important to human health. Shonhai's group published a review article regarding the roles of the Heat Shock Proteins (HSP) acted as immunomodulates whose capability is to transform the anti-inflammatory property when the HSP concentrations are low to the pro-inflammatory property when HSP concentrations are high [5], and unfortunately the authors did not define the concentration range. We felt an unmet need exists for this health-related important topic. Extracellular ATP concentration and intracellular ATP concentration ranges are important related to HSPs' functions either in physiological or pathological function, because HSPs primarily occur extracellularly, but also reported from literature, HSPs occur in an intracellular micro-

environment [6]. If we can build a well-characterized and well-controlled system to define the critical HSP concentration ranges in the transformation between the two statuses that would be a primary attempt toward a resolution.

Recent theoretical predictions of Josephson-based meminductive, memristive quantum superconducting devices have drawn an attention [7-9] that the Josephson supercurrent behaves hysteretically, herein our group reported a unique type of nanostructured organo-metallic devices developed, named as Sensor 1, for the purpose of mimicking the active state of Matrix Metalloproteinase-2 (MMP-2), which is able to directly interacting with ATP by a heating method, and compared with a manmade activated biomimetic MMP-2 Sensor 2 by direct depositing the mixtures on the gold chip surface, that enabled us to quantitatively detect 100 aM to 60 nM ATP in two types of milk samples by a Chronoamperometric method (CA) and an Open Circuit Potential method (OPO) [10]. The goal of this report is to focus on the method development for assessing the ATP concentrations effect on the RMP with or without LPS influences compared with controls by using the newly developed sensors.

2. Results and Discussions

2.1. The Friedel-oscillation in the Superlattice Membranes

Friedel-oscillation is a phenomenon of long-range indirect interactions between electrons on a superlattice surface [11]. Evaluations of the Friedel-oscillation were conducted based on the AFM images. Fig. 1 revealed the strong Friedel-oscillation with a flame-like electronic cloud surrounded on the zinc atoms in which the "cloud" moves toward the same direction in the 1.0 μm^2 area. This is the evidence of the Cooper pair transmission waves happened at the Josephson junction. The image was for the biomimetic “native” MMP-2 membrane, i.e., the membrane comprised of triacetyl-ß-cyclodextrin (TCD), polyethylene glycol diglycidyl ether (PEG), poly(4-vinyl pyridine) (PVP), bis-substituted imidazole dimethyl-β-cyclodextrin (bM-β-DMCD), cysteine and embedded zinc chloride in appropriate proportions. The native MMP-2 protein has two states: an innate state with the cysteine “on” and an activated state with the cysteine “Off”. Fig. 1 was with the cysteine "On" in its innate state, and we observed the Cooper pair electrons moving toward the same direction. Sensor 1 has an activated biomimetic MMP-2 membrane by a heating method to kick out the cysteine group in the network, as evidence, we did not observe moving Cooper pairs in Fig. 2, the labeled square has the same Z range as shown in Fig. 1. The matrix of the superlattice was shown partially damaged shown in Fig. 2. Sensor 2 was directly fabricated using bM-β-DMCD, TCD, PEG, PVP and $ZnCl_2$, except without cysteine. The Friedel-oscillation was observed in two locations in Fig. 3(a) (0.734×0.734 μm^2) and Fig. 3(b) (0.9×0.9 μm^2). Fig. 3(a) shows the cylinder-shaped structure formed on the membrane comprised of an array of multiple-layer rings with a cavity on average 500 nm diameters, where clusters of zinc atoms as the Josephson junction (JJ) connected to the rings. Fig. 3(b) depicts the Friedel-oscillation observed as the moving flames surrounded the zinc atoms, while the Cooper pairs moved toward the same direction and the superlattice matrix was very orderly arranged on the surface. Fig. 3(c) depicts the large area formation of the tall cylinder structure in 3.8×3.8 μm^2 from the top view, and the center cavity is 1.3-1.5 μm diameter. Zinc atoms were seen on the top surface and the edge. Fig. 3(d) depicts the side view of the cylinder-shaped structure having 491 nm in height and sitting on a flat area in 10×10 μm^2. It may assemble the HSP60 unique 3D-cage cylinder structure with 7 asymmetric subunits. Fig. 3(b) was shown in the flat area.

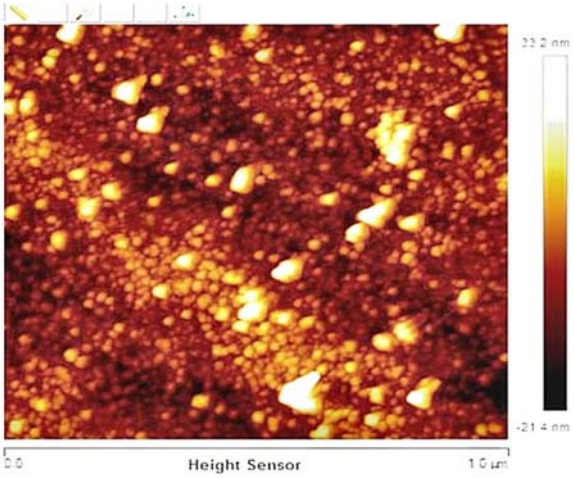

Fig. 1. AFM membrane image in the native state.

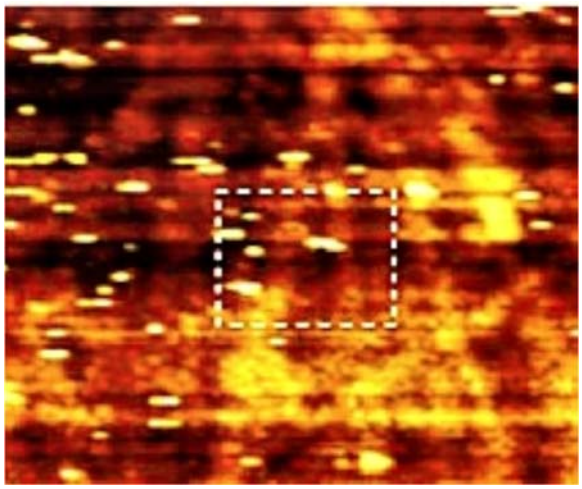

Fig. 2. 3D image of the activated Sensor 1 by a heating method.

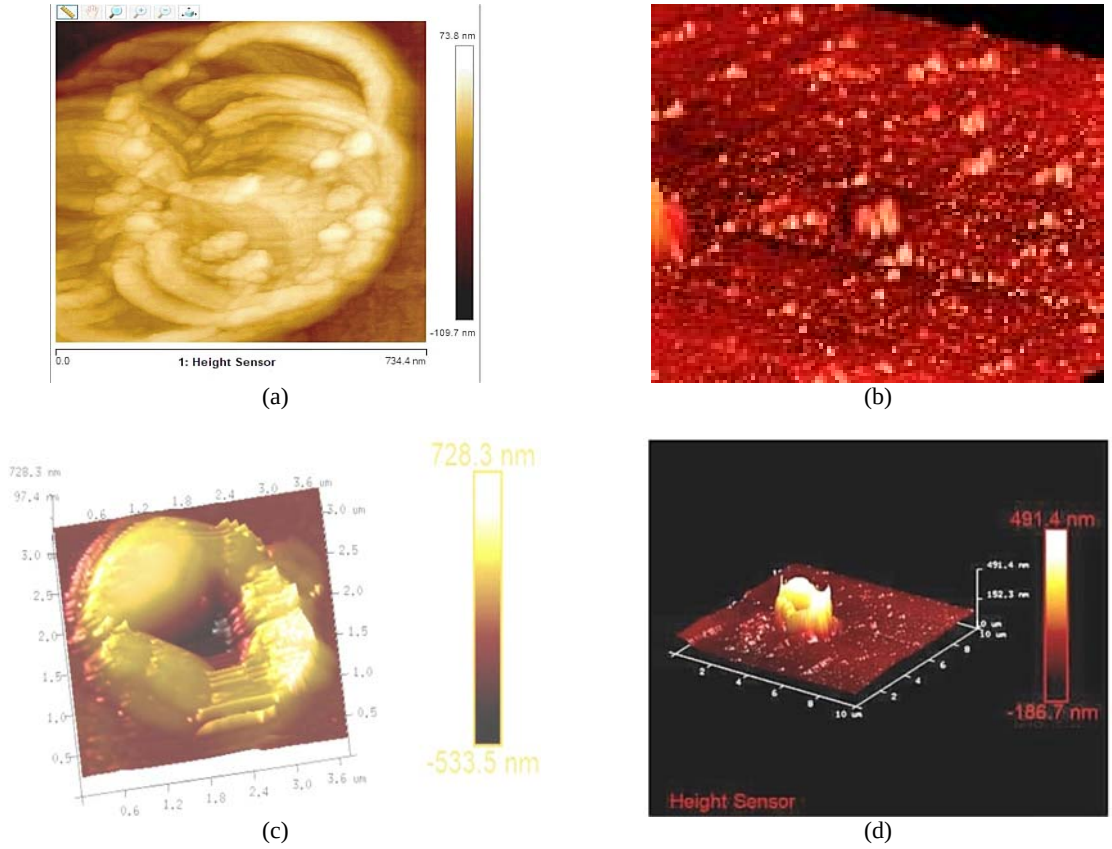

Fig. 3. (a) Image of the multiple-layer ring structure of the activated Sensor in 0.734×0.734 μm^2, (b) Enlarged image in 0.9×0.9 μm^2 shown in the flat area in (d), (c) Enlarged top view of the cylinder shown in (d), (d) Side view of the cylinder in 10×10 μm^2.

2.2. The Proposed Mechanism of Testing the Extracellular ATP in Biological Specimens Using the "Stressful" Biomimetic MMP-2/HSP60 Sensing Device

To make direct quantitatively testing ATP in the biological specimen under antibody-free and label-free conditions, the challenge we are facing is to overcome the instability of ATP, and also to overcome the weak long-distance communication between the functional groups in the 3D cage membrane and the ATP molecules in the biological media. One of the ideas is to make ATP molecules to be protected in an imidazole modified cyclodextrin (CD) cavity, which contains a trunked "donut" porous structure with inside hydrophobic and outside hydrophilic properties, and forms an inclusion "Guest-Host" complex in the media [12-13]. When the complex moves nearby the 3D cage membrane, the zinc cations and imidazole groups in the membrane may provide a force to attract ATP. Therefore, the bio-communication of ATP can be quantified. The proposed steps of the ATP communication with functional groups are listed:

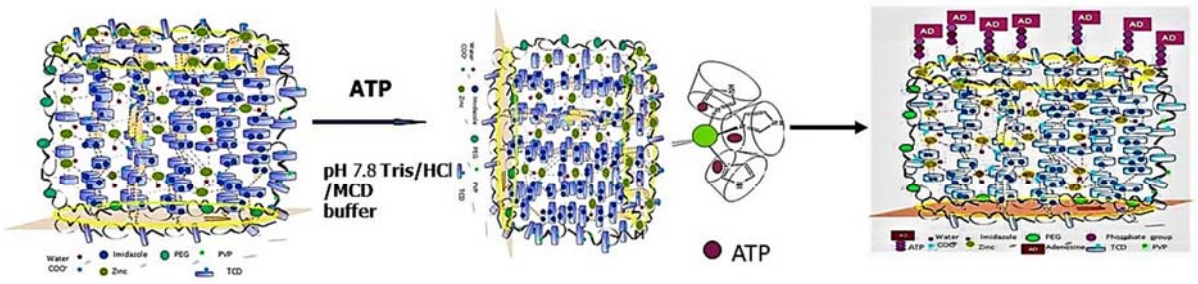

Step 1, form the DET relay; Step 2, form a long-range DET relay, and Step 3, ATP direct communicates with the Functional groups in the 3D cage membrane.

3.1. Comparison of the Performance for ATP Sensing Using the CV Method

Low scan rate. Evaluation of the ATP sensing performances in the buffer media between the two types of sensors was conducted using the CV method. The characteristics of memristive hysteresis curves were observed in Fig. 4(a) for Sensor 1 with the scan rate changes from 1 Hz to 25 kHz in the control media and without ATP, and compared with current exponentially increase curves observed in Fig. 4(b) in both Direct Electron Transfer in DET_{ox} and DET_{red} peaks at ATP concentration from 40 fM to 60 nM compared with the control having 66.5, 146, 3048.7 and 4664-fold increase for DET_{red}, respectively at 60 Hz scan rate. There was no superconductivity observed. The calibration curve is shown in Fig. 4(c) has a power of 0.3 that indicates the current increase rate is 30 % of the rate in ATP concentration increase after conversion from the double log plot.

Fig. 5(a) depicts the control media CV curves for Sensor 2 with the scan rate from 1 Hz to 25 kHz. Sensor 2 demonstrated a perfect memristive behaves at 60 Hz and also showed the superconductivity at zero-bias potential over the scan rate from 5 kHz to 25 kHz with phase change and oscillation. This observation explained that the Cooper pair electron cloud formation (image Fig. 3(a) and Fig. 3(b)) is a key to the superconductivity. Sensor 2's sine or cosine wave peak superconducting current intensity increased or decreased exponentially for forwarding scan and backward scan, respectively, over ATP concentrations from 400 aM to 2 μM at zero-bias with 60 Hz scan rate as shown in Fig. 5(b). The superposition characteristics as an example are labeled in Panel F in Fig. 5(b). Using Sensor 2, the ATP concentration change from 25 aM to 400 aM demonstrated a unique capability to turn the memristive to superconductive at a lower scan rate 60 Hz compared with the control that has the only memristivity. Fig. 5(c) shows the superconducting current curves vs. ATP concentrations for the forward and backward scan, respectively. The power of the current vs. ATP concentration with the forward scan is 50 % of that of the Sensor 1, however, it also indicates the superconductivity was solely induced by the mem-inductance through the Josephson junction at zero-bias.

High Scan Rate. At a 10 kHz scan rate, Sensor 2's superconducting current increased at zero-bias from Panel B to Panel I, is exponentially proportional to the ATP concentrations from 200 fM to 200 μM compared with the control shown in Panel A of Fig. 6. By plotting the calibration curve of superconducting current vs. ATP concentrations in the forward scan and the backward scan at 10 kHz as shown in Fig. 7(a) and Fig. 7(b), respectively, we obtained the power of 3.75 after conversion from the semi-log plot, which means the current increase rate is 3.75-fold higher than the ATP concentration increase rate. This 3.75 power is more than 12.5 and 27-fold higher than Sensor 1 and Sensor 2 at 60 Hz scan rate, respectively.

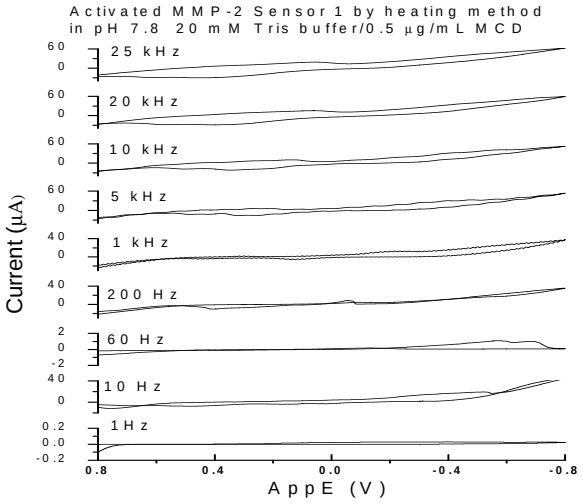

Fig. 4 (a). Sensor 1's i-V curves in different scan rate in the Tris/HCl/MCD buffer.

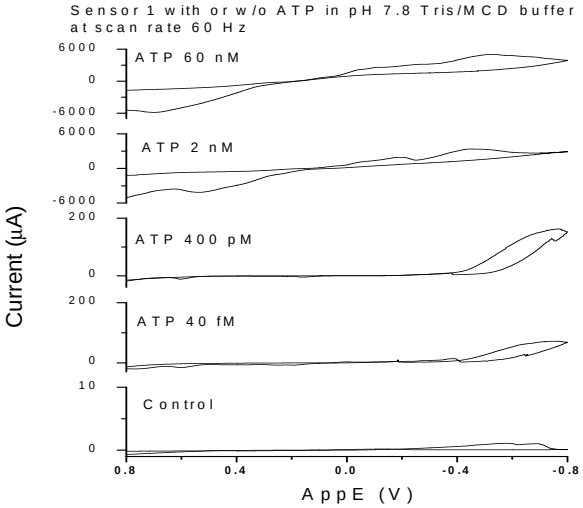

Fig. 4 (b). Sensor 1's i-V curves under the influence of ATP concentrations compared with the control.

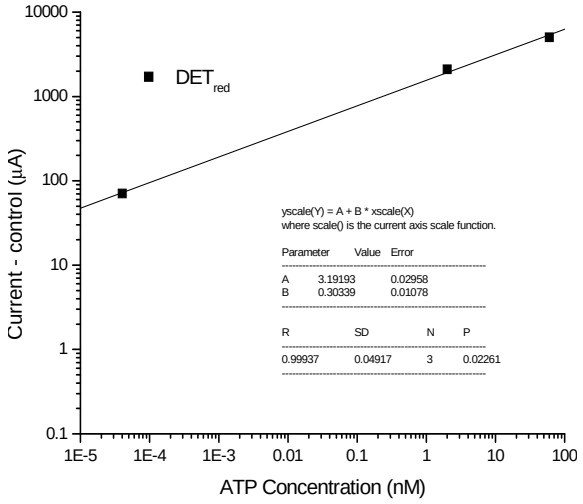

Fig. 4 (c). Calibration curve with a double-log plot for the DET current vs. ATP concentrations using Sensor 1 in the buffer.

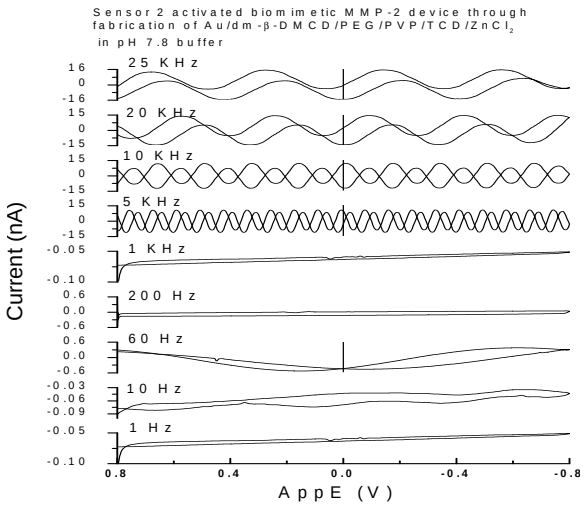

Fig. 5 (a). Sensor 2's control i-V curves under same conditions as the Sensor 1 for controls.

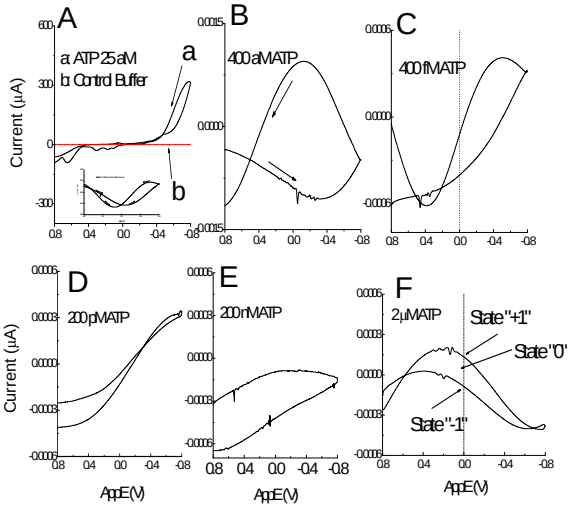

Fig. 5 (b). Sensor 2's i-V curves under the influence of ATP from 25 aM to 2 μM compared with the control using a 60 Hz scan rate.

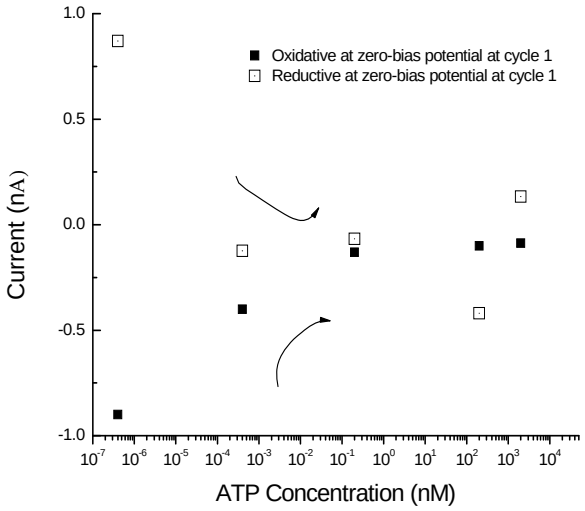

Fig. 5(c). Plots of current vs. ATP concentrations of Sensor 2.

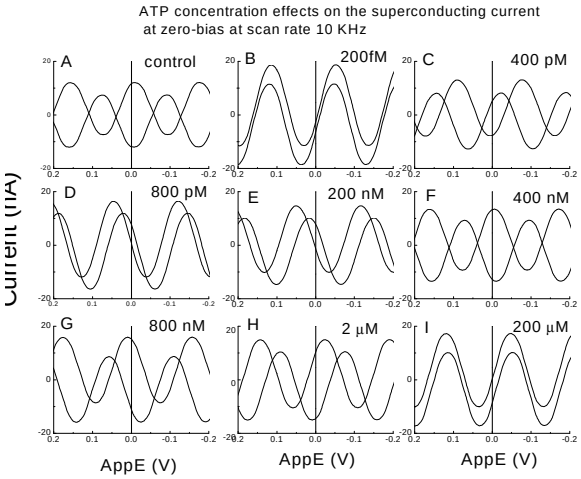

Fig. 6. CV curves of current vs. applied potential at 10 kHz scan rate with ATP concentration from 200 fM to 200 nM against the control.

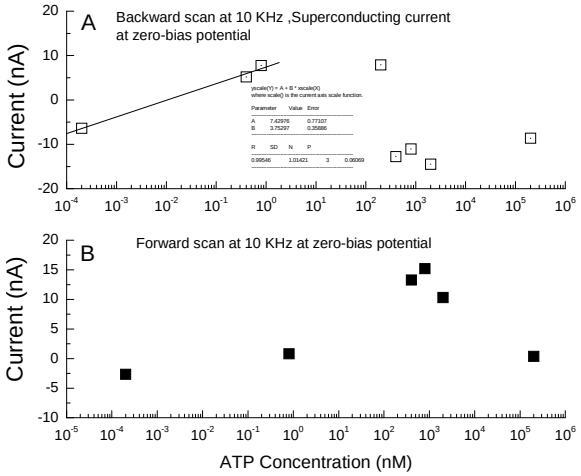

Fig. 7. Curves of superconducting current vs. ATP concentrations for the forward scan 10 kHz (b) and backward scan (a).

3.2.1. Define the Immunomodulant Concentration Effect on Transformations from Anti-inflammatory to Pro-Inflammatory Using the CV Method

We used the Sensor 2 system, which mimics the physiological HSP60 in the presence of ATP gradient concentration between 200 fM to 800 nM, the superconducting current is in the exponential increase with an anti-inflammatory status, and from 1 μM and higher, the superconducting current dramatically drops down, indicates the system is in a pro-inflammatory status as shown in Fig. 7(a) and Fig. 7(b), respectively. Because the biomimetic HSP60 concentration in the sensor membrane was fixed, hence the biomarker for the HSP60 concentration will be represented by the superconducting current dramatically turning point associated with ATP concentrations.

3.2.2. A 3D Map Method Used for Defining of the Transformational Status of the Immunomodulant

In this section, the multiple variables, such as the ATP concentration, the applied potential effect on the quantum conductance were studied through the 3D mapping method without decomposed the superconducting energy into several components. Fig. 8 depicts the 3D dynamic map of the relationships over 5 level ATP concentrations from 0.2 pM to 2.0 µM over the potential range between -40 mV to +40 mV to illustrate the relationship among ATP concentrations, zero-bias potential and the differential quantum conductance using 10 kHz scan rate forwarding scan data. From the map, the quantum conductance values are correlating with the ATP concentrations at zero-bias, except at a higher concentration near 1.0 µM, it was dropped. We primarily suggest the turning point of the ATP concentration from anti-inflammatory to pro-inflammatory for a "healthy" Biomimetic MMP-2/HSP60 Sensor 2 in the extracellular environment is higher than 800 nM. Fig. 9 further shows a contour map relationship between the ATP concentration (as the y-axis), and the applied potential (as the x-axis) and the quantum conductance (as Z-axis). It was observed that the range between the highest quantum conductance values at zero-bias is associated with the ATP concentration between 200 fM to 800 nM, so we define this range having the Physiological High-Frequency Oscillation (pHFO) as the "Anti-inflammatory" range; when concentration higher than 800 nM, the quantum conductance values are reduced, and this range was defined as the "Pro-inflammatory" in the extracellular ATP concentration range at 10 kHz.

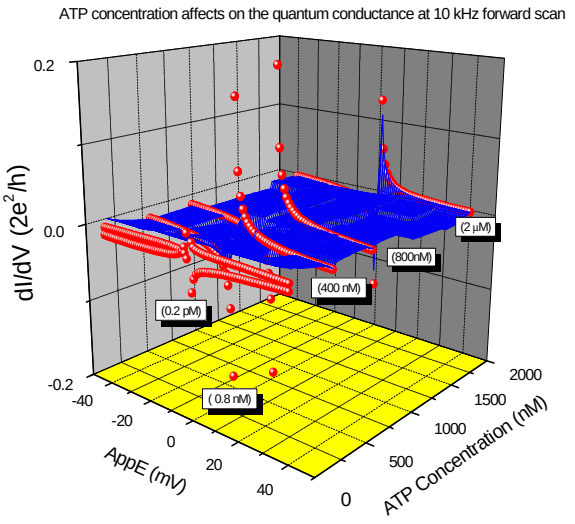

Fig. 8. 3D dynamic map of the relationships over 5 level ATP concentrations from 0.2 pM to 2.0 µM over the potential range between -40 mV to +40 mV for the relationship among ATP concentrations, zero-bias potential and the differential quantum conductance using 10 kHz scan rate.

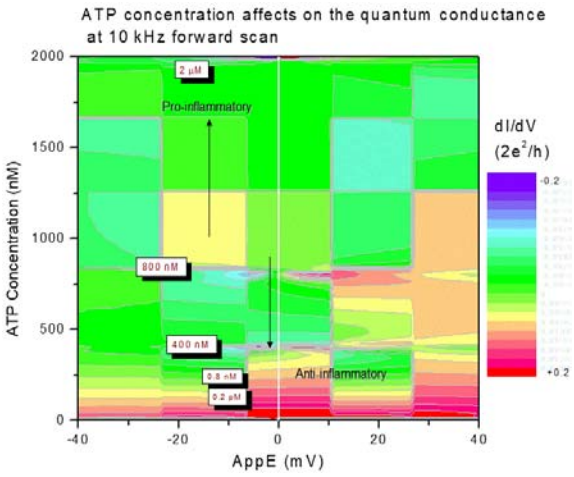

Fig. 9. Anti-inflammatory and the Pro-inflammatory counter map related to the ATP concentration, zero-bias and the quantum conductance for the "Healthy" HSP60 Sensor 2.

Because Sensor 1 can be viewed as a "Mutated" or "Stressful" Biomimetic MMP-2/HSP60 model as far as the capability to promoting the Cooper-pair electrons' concerns, was greatly diminished as shown in Fig. 2, hence it was shown Sensor 1 neither have superconducting peaks in the presence of ATP in the buffer media in 60 Hz and 10 kHz scan rate, respectively.

3.2.3. Define the Immunomodulant Concentration Effect on Transformations Between Pro-Inflammatory and Anti-inflammatory Status Using an Open Circuit Potential (OPO) Method

Above Sections used a potentiostat method to study the extracellular ATP concentration effect on the transformation between Anti-inflammatory and Pro-inflammatory status as far as the ATP concentration concerns, and this section uses a galvanostat method to study the two status transformations spontaneously happened intracellular ATP concentration change caused net energy change compared with the control in the buffer media under an open circuit condition. Sensor 2's strong superconductivity has enabled the device to direct real-time monitor energy change under open circuit potential, under a reagent-less and antibody-free condition. Fig. 10 depicts the voltage curves exponentially increase as the ATP concentration increase compared with the control in the media. Fig. 11 depicts the non-linear calibration curve of voltage vs. concentrations over the range of 25 aM to 400 pM. Fig. 12 plots for high-end ATP concentration curve voltage profiles over 0.8 nM to 2 µM. The voltage results showed the intracellular ATP transformational point concentration between the anti-inflammatory and the pro-inflammatory is in the range higher than 0.4 nM, for example, at 0.8 nM, the

energy drop with a first-order rate of 0.01 V/nM decay that indicates the intracellular ATP concentration is too high pathologically. Fig. 13 shows the voltage vs. concentration double-log plot with a logistic fitting curve whose power of 0.66 indicates the intracellular high ATP concentration increase rate is too high may not be able to sustain a constant cell RMP that leads to pro-inflammatory.

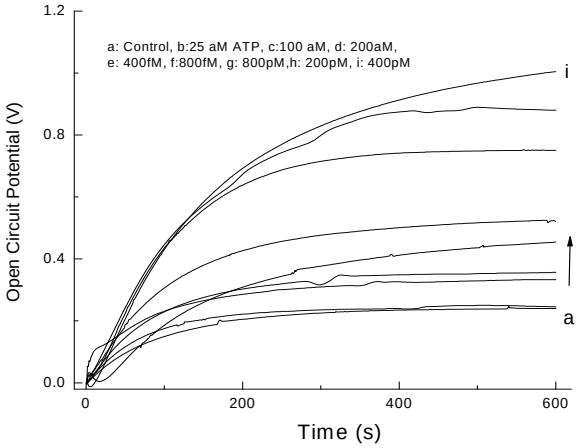

Fig. 10. Sensor 2 ‘s open circuit potential curves for monitoring the energy change over 25 aM-400 pM ATP compared with the controls.

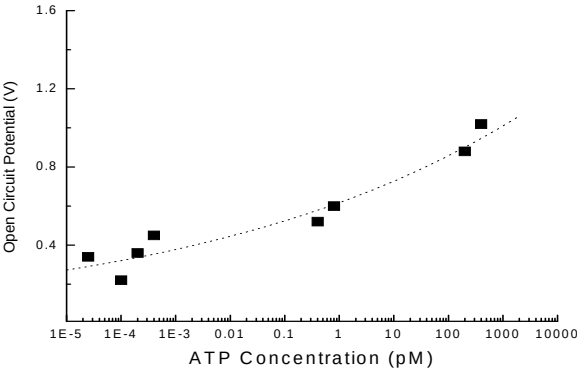

Fig. 11. Open circuit potential curve vs. ATP concentrations over 25 aM to 400 pM.

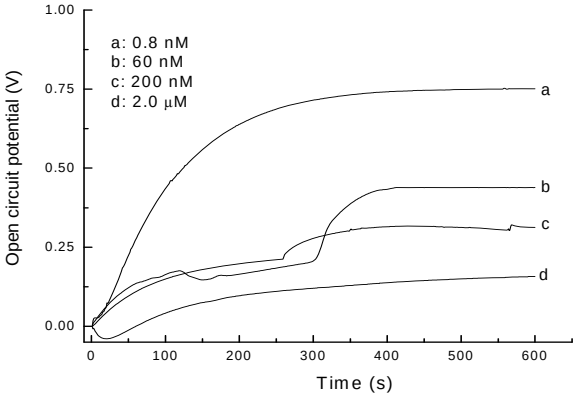

Fig. 12. Open circuit potential curves vs. time over ATP concentration range from 800 pM to 2.0 μM in the buffer media.

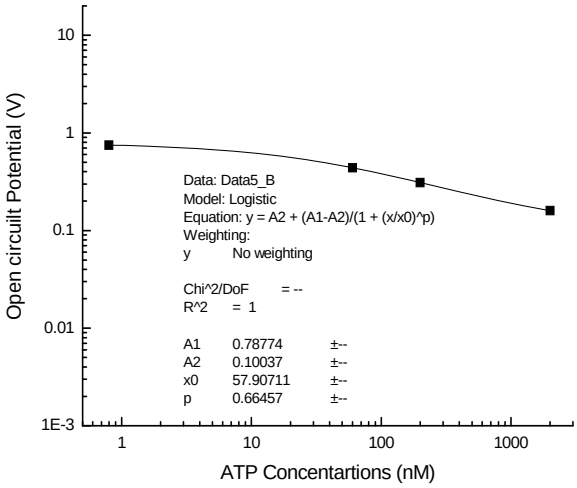

Fig. 13. Calibration curve over this range addressed in Fig. 12.

4. Assessing Human Milk Immunological Advantage in Preventing Extracellular ATP Hydrolyzation

X. Chen's group reported ATP hydrolyzation extracellularly induces cancer cells drug resistance [1-4]. Assessing human milk immunological advantage in preventing extracellular ATP hydrolyzation is important. Our study was conducted through the CV method using the Sensor 1 because we knew Sensor 1 lacks Copper-pair electrons, and we used the human milk samples compared with the certified organic milk samples for infants under the same experimental conditions. Fig 14 (Left) shows the extracellular hydrolysis DETox curves (as also called the memristive peak) happened in the presence of spiked 60 nM ATP (final concentration), which caused a 9-fold increase of the peak current at 700 mV compared with the organic milk negative control. There is an unknown peak observed in the organic control milk sample located at 20 mV, and the peak was the 2.8-fold increase of the amplitude when ATP presences. In contrast, Fig. 14 (Right) shows the buffer control sample of the CV curve has no such unknown peak at 20 mV.

There is a current increase for the DET_{ox} peak at 700 mV for more than 173-fold in the presence of 60 nM ATP compared with the control, and the DET_{red} peak intensity also increased 150-fold in the presence of ATP compared with the control buffer sample. The DET_{ox} has a first-order ATP hydrolysis rate of 5.92×10^{-3}/s by plotting the peak currents vs. scan cycles (each cycle is 53.33 s) as shown in Fig 15. The top curve is for the DET_{red} peak current vs. scan cycles; the bottom curve is for the DET_{ox} peak current vs. scan cycles.

Human milk samples communicated with the “mutated” HSP60 membrane on the same Sensor 1 having a different manner compared with the organic cow milk samples. Figs. 16, 17, 18 and 19 depict the human milk samples under the impact of 60 nM ATP

concentration in 4 scan cycles (2 more cycles curves did not show) compared with the human milk controls using Sensor 1 at 60 Hz. The nodes, the super-positioning and the phase change at the zero-bias were observed, and there was no ATP hydrolysis signature peak observed, and there was no unknown DET reduction peak noticed. Fig. 20 shows an alternative up and down peak superconducting current vs. scan cycles for the forward and backward scan, respectively. The human milk samples have "eyes" that can see the danger and purposely avoiding communicate with the ATP molecules because in the human milk contains living microbiota, which the HSP60 and ZnT chaperonin proteins in the extracellular plays a role of the guardian's protection.

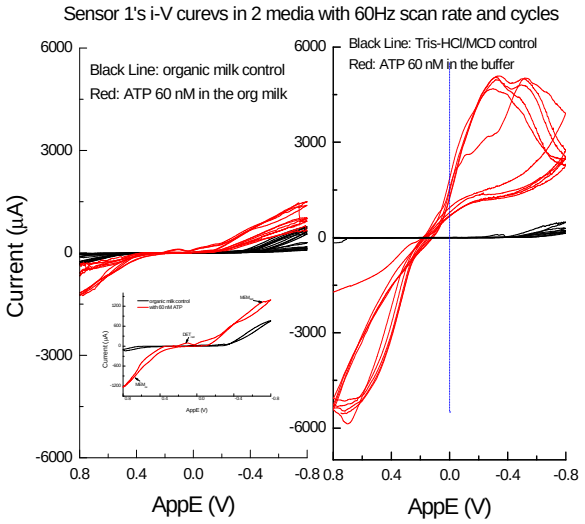

Fig. 14. (Left). Organic milk CV curves for current vs. applied potential in the presence of 60 nM ATP compared with the milk control (in black color) in 6 consecutive scans at 60 Hz. (Right) CV curves of with 60 nM ATP (in red color) in buffer media and curves of the buffer control.

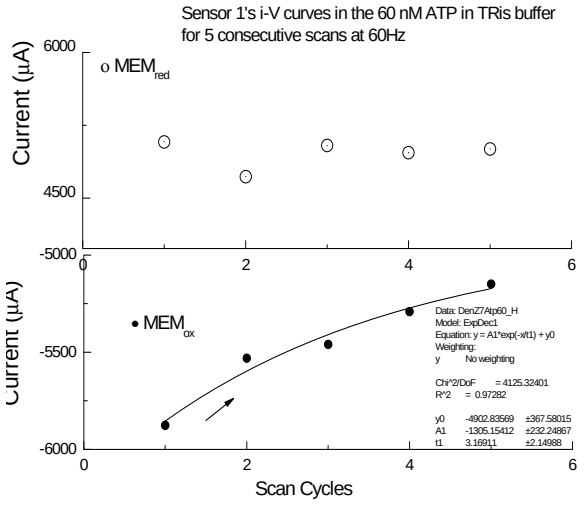

Fig. 15. DET peaks current vs. scan cycles: top panel is for the DET_{red} peak and the bottom panel is for the DET_{ox} peak.

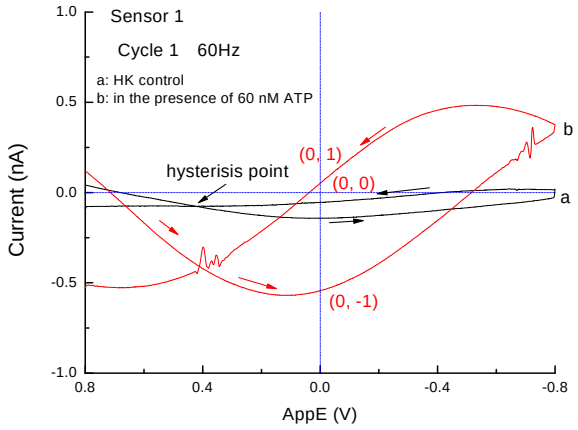

Fig. 16. First scan cycle at 60 Hz in the presence of 60 nM ATP (final concentration) in human milk sample compared with the milk control sample.

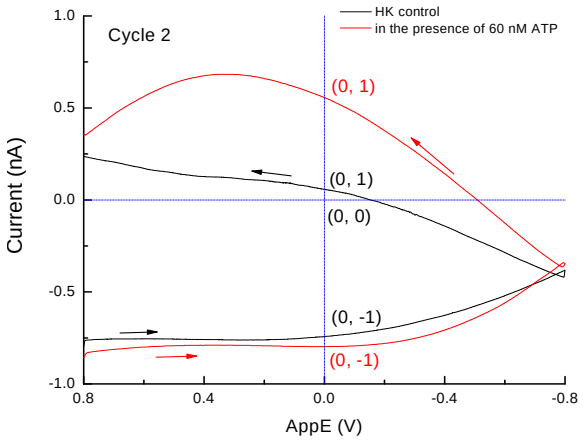

Fig. 17. Second scan cycle at 60 Hz in the presence of 60 nM ATP (final concentration) in human milk sample compared with the control milk sample.

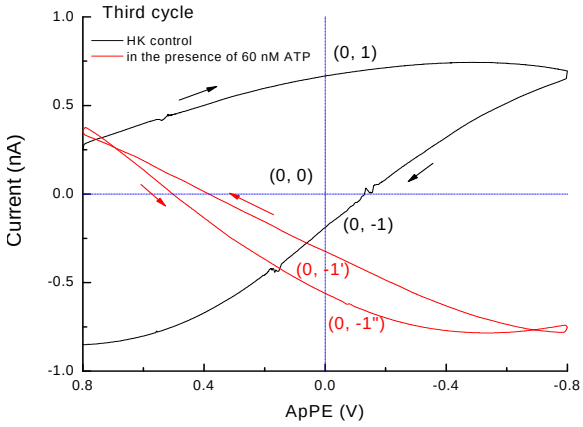

Fig. 18. Depicts the third scan cycle.

Fig. 21 shows the overlapping curves of the control human milk sample in 6 consecutive scans vs. the milk sample with 60 nM ATP. The peak magnitude kept the same, but the phase change is constantly happening for with or without ATP, that indicates the human milk promoting an orderly electromagnetic energy stored in the cell for enhancing the brain development and memory caused by the meminductivity through the

Josephson junctions, in which is advantages compared with the "chaos" electromagnetic energy acquired from Alzheimer's β-amyloidal accumulation [14-17].

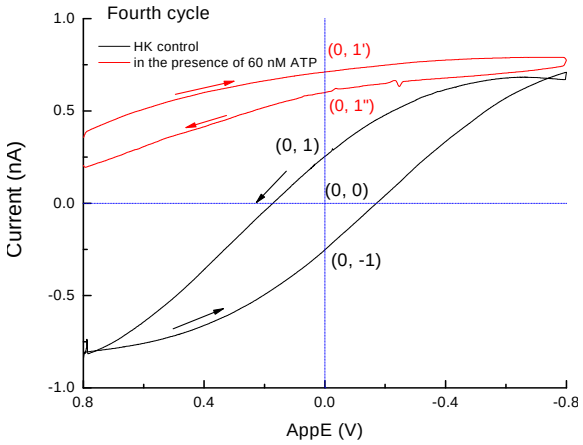

Fig. 19. Fourth scan cycle.

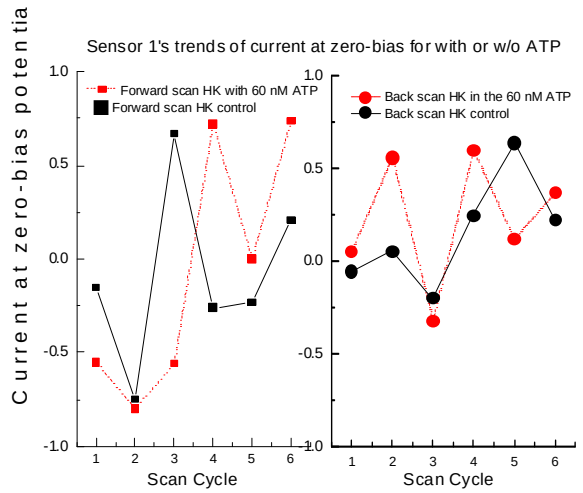

Fig. 20. Alternative trends of the superconducting current at the zero-bias vs. scan cycles for the forward scan and backward scan compared with the human milk controls, respectively.

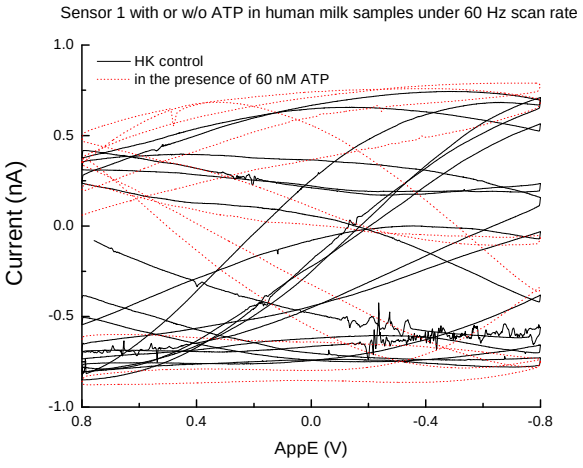

Fig. 21. Overlapping curves of the control human milk sample in 6 consecutive scans vs. the milk sample with 60 nM ATP at 60 Hz.

5. Quantitation of ATP by Sensor 2 Using the Voltage Method

5.1. Curves of Voltage Values vs. ATP Concentrations

The Double Step Chronopotentiometry (DSCPO) method, i.e., the voltage method was used for study of the quantitative detection of ATP in biological specimens. Fig. 22 shows the voltage vs. time curves at 0.25 Hz at ±10 nA over the ATP concentrations from 25 aM to 400 nM against the control samples with each sample run triplicates using Sensor 2 in the Tris buffer solution. Fig. 23 shows the calibration curve of a semi-log plot for the normalized action potential vs. ATP concentrations, and it produced an equation having a power of 0.06, r=0.99 (n=18), P<0.0001, over ATP concentration from 100 aM to 200 nM with a relative standard error of estimation of 2.0 %. Fig. 24 shows the semi-log plot of the absolute normalized resting potential vs. ATP concentrations having a power 4.39 indicated resting potential effect at ATP concentration lower than 100 aM is dominate than that of the action potential effect.

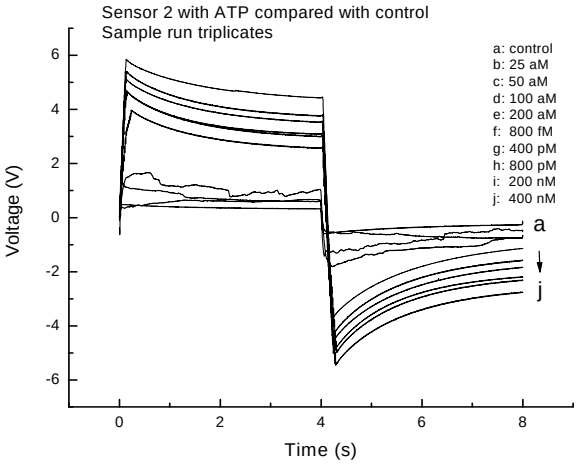

Fig. 22. Voltage curves in 9 ATP concentration levels from 25 aM to 400 nM compared with the control buffer samples at ± 10 nA with step time 4 s using Sensor 2.

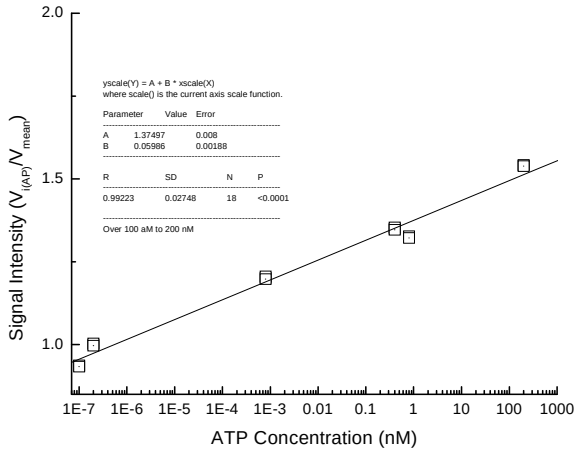

Fig. 23. Semi-log. plot of the normalized action potential values vs. ATP concentrations.

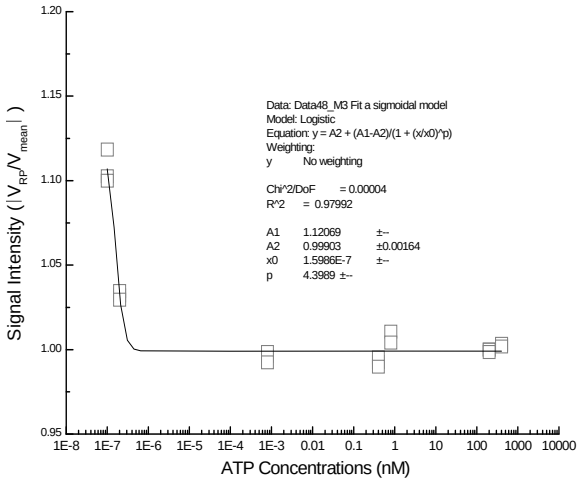

Fig. 24. Semi-log. plot of the absolute normalized resting potential vs. ATP concentrations.

5.2. Define ATP Concentration Ranges Effecting on Cell Membrane Potential and its Ratio

It is a well-recognized phenomenon that cancer cells have abnormal cell membrane potential [18-21]. Biologists measure cell membrane action and resting potentials with burdensome instrumentation and time-consuming procedures. A recent report shows breast cancer cell division caused a membrane potential increase [21] due to variations in ion channel expression. Because the normal cell membrane action potential is 58 mV, and -70 mV is for the resting potential [22], the small signals are very easily buried in the background noises [23] that can cause problems to pediatric neurologist and intensive care unit doctors who need strong signals to monitor and diagnose the neonatal neurological diseases [23]. The consequences of human cancers, trauma brain injury (TBI) and other diseases are not be able to maintain mitochondrial cell's reversible membrane potential (RMP) and unable to maintain the normal membrane's potential ratio between the action potential and the resting potentials [18-27]. Our group first used the biological marker of the action/resting potential ratio to monitor the treatment of triple-negative breast cancer and the brain cancer prognosis in a 3D heat release map [24-27]. There is very few, if any, uses the ratio of action/resting potential as a biomarker to monitor and define the ATP concentration ranges, that transforms from anti-inflammation to pro-inflammation in the presence of bacterial toxins under a well-controlled system without any sample processing, no labeling and no tracers were used. Fig. 25 shows the cell RMP voltage (after subtracting the control) is not depending upon the ATP concentrations between the range from 100 aM to 800 nM with a power of 0.013, that means the cell voltage increase rate is only 1.3 % of the ATP concentration increase rate, hence this range is the "safe zone" confirmed by Fig. 7 using the 3D map method based on the CV data. However, we found concentrations lower than 100 aM and higher than 800 nM the cell RMP can not keep constant, either lower than the normal average cell voltage, or 10, 20-fold higher than the normal average cell voltage, therefore, we define this range as the pro-inflammatory toxin range, for contrast, the "safe zone" range was defined as the anti-inflammatory toxin range.

Fig. 26 further shows the extracellular ATP concentration range effects on the ratio of the cell action potential vs. resting potential. The results showed the concentration lower than 100 aM or higher than 400 nM will lead to a ratio of action vs. resting potential either significantly lower or significantly higher than the normal ratio range, which is between 0.7 to around 1.0 [8-11]. Our prior works revealed the living cancer cells can lead to an abnormal ratio up to 3, 10 to 100-fold higher than this range according to the nature of cancer and the stage of the cancers are in. Even Fig. 25 reveals the total cell voltage at 800 nM is in the "safe zone" is respected to the energy concerns, but clinically, the ratio value in Fig. 25 further revealed the 800 nM ATP concentration led to a 10-fold higher than the normal ratio range, hence in Fig. 26 we excluded the 800 nM points. The ratio vs. concentration curve has a power 0.08 that means the ratio increase rate is 8 % of the concentration rate increase having a CV value ±4.5 % error in the normal range was demonstrated.

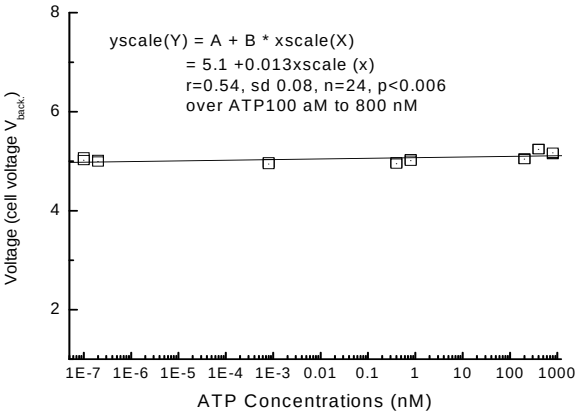

Fig. 25. ATP concentration ranges effect on the cell membrane potential.

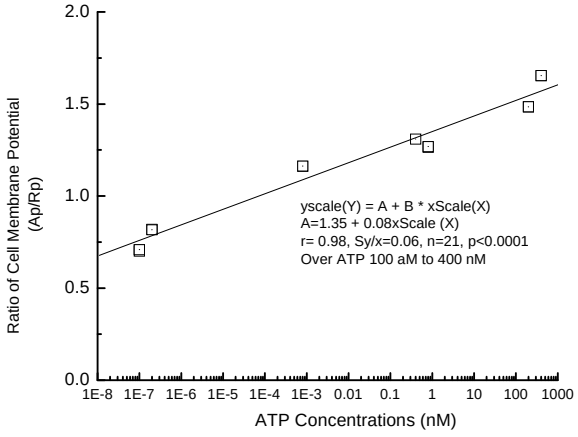

Fig. 26. ATP concentration ranges effect on the ratio of action potential vs. resting membrane potential.

6. Point Accuracy and Imprecision

Point accuracy and imprecision was studied through the recovery experiments using spiked human milk and the USDA certified organic milk samples against the control samples with 2 levels of ATP concentrations at 100 aM and 60 nM, respectively. We compared the measured results with the calibration curve after subtraction of the voltage values from control samples using Sensor 2 as shown in Table 1. We also studied the LPS effects on the recovery at 10 fg/mL and 90 fg/mL, respectively under a fixed ATP concentration of 60 nM. The results shown the recoveries using human milk and organic milk samples with the voltage method are higher than 96 % with an imprecision error less than or equals to 2 % at the 100 aM and 60 nM levels ATP compared with the controls, respectively without LPS challenge. Using two levels of LPS challenges with the fixed ATP 60nM, the recoveries are 103±0.8 %, 103±0.7 % for human milk samples compared with the spiked controls at the same level in the buffer; using organic milk samples, the recoveries are 97±1 %, 18.8±0.3 % at 10 fg/mL LPS and 90 fg/mL LPS, respectively traced back to the spiked controls at the same level in the buffer. These results showed organic cow milk samples are vulnerable to the LPS attack in higher-level 90 fg/mL, which caused an unacceptable result in recovery, but the human milk samples demonstrated immunological advantage with 100 % recovery with two levels LPS challenges even under 60 nM ATP concentration.

Table 1. Comparison of the Method Performance for Quantitation of ATP Spiked in the Milk Samples using the voltage method.

ATP Recovery (% (sd))				**HSP60-effect (% (sd))**	**Sample type**
Without LPS		**With LPS challenge**			
Low ATP	**High ATP**	**Low LPS**	**High LPS**		
100 aM	60 nM	10 fg/mL	90 fg/mL		
98.6 (1.0)	96.5 (0.14)	103 (0.8)	103 (0.7)	0 (0.3)	HK
98.6 (0.8)	96.8 (2.0)	97.0 (1.0)	18.8 (0.3)	0 (0.2)	OK

For with LPS, ATP=60 nM. The whole cell voltage data were used. HK: human milk; OK refers to the organic milk samples.

7. Experimental

Sensor 1 has an activated biomimetic MMP-2 membrane by a heating method at 80°C for 5 minutes using the innate biomimetic MMP-2 membrane fabricated based on a published procedure [28]. Sensor 2 was also in a state of activation of biomimetic MMP-2 by a direct deposited method with compositions of TCD, PEG, PVP, bM-β-DMCD and embedded zinc chloride on gold chips with appropriate proportions at 37°C for 96 hours. The USDA certified organic milk for infants was compared with human milk (Lee Biosolutions, MO) without prior sample preparation. Human milk was collected from normal subjects who breastfeed 1-month-old newborns, each sample run triplicates.

The morphology of the AU/SAM was characterized using an Atomic Force Microscope (AFM) (model Dimension Edge AFM, Bruker, MA). Data collected in TappingMode using silicon probes with a 5-10 nm tip radius and ~300 kHz resonance frequency (Probe mode TESPA-V2, Bruker, MA).

8. Conclusions and Discussions

ATP concentrations affecting the anti-inflammatory and the pro-inflammatory status was demonstrated using organo-metallic devices from the anti-inflammatory to pro-inflammatory in the extracellular environment and the intracellular environment by directly testing ATP in the biological specimen samples using various methods. The ATP molecules were able to be stabilized in the Tris buffer and MCD media promoted a long-range DET favorable status led the ATP molecules directly communicate in the 3D-cage Biomimetic MMP-2/HSP60-like membrane, that stimulated superconductivity at the gamma frequency 60 Hz over 400 aM to 2 μM without causing any extracellular ATP hydrolysis using the human milk measured by Sensor 1 compared with the organic milk samples, that have significant ATP extracellular hydrolysis under the same experimental condition, here human milk offers immunological advantage with proven pieces of evidence. At the ATP concentration 100 aM, both milk samples have offered acceptable more than 96 % recoveries with good agreement imprecision using the Sensor 2 of the voltage method indicate the nanostructured 3D-cage biomimetic MMP-2/HSP60 membrane design offered a pathway leads to a rapid real-time precise monitoring bacterial contamination in the future.

Acknowledgments

We thank Matt Lee and his team for recruiting and providing human milk samples as gifts for our projects. E. Chen thanks Dr. Kasica's help and discussions and thanks to the NIST NanoLab for the cleanroom and other equipment.

References

[1]. X. Wang, Y.-S. Li, Y. Qian, *et al*., Extracellular ATP, as energy and phosphorylating molecule, induces different types of drug resistance in cancer cells through ATP internalization and intracellular ATP level increase, *Oncotarget*, Vol. 8, Issue 50, 2017, pp. 87860-87877.

[2]. J. Gu, J. S. Wiley, Rapid ATP-induced release of matrix metalloproteinase 9 is mediated by the $P2X_7$ receptor, *Blood*, Vol. 107, Issue 12, 2006, pp. 4946-4963.

[3]. A. Manica, A. M. Da Silva, A. M. Cardoso, High levels of extracellular ATP lead to the chronic inflammatory response in melanoma patients, *J. of Cellular Biochemistry*, Vol. 119, Issue 5, 2018, pp. 3980-3988.

[4]. A. P. S. Bertoni, R. P. De Campos, M. Tsao, *et al*., Extracellular ATP is differentially metabolized on papillary thyroid carcinoma cells surface in comparison to normal cells, *Cancer Microenviron*, Vol. 11, Issue 1, 2018, pp. 61-70.

[5]. T. Zininga, L. Ramatsui, A. Shonhai, Heat shock proteins as immunomodulators, *Molecules*, Vol. 23, Issue 11, 2018, pp. 2846.

[6]. P. G. Jobin, G. S. Butler, C. M. Overall, New intracellular activities of matrix metalloproteinase shine in the moonlight, *BBA-Molecular Cell Research*, Vol. 1864, Issue 11, Part A, 2017, pp. 2043-2055.

[7]. S. Peotta, M. Di Ventra, Superconducting memristors, *arXiv:1311.2975v2*, 2014.

[8]. J. Salmileto, F. Deppe, M. Di Ventra, Quantum memristors with superconducting circuits, *Scientific Reports*, Vol. 7, 2017, pp. 42044.

[9]. C. Guarcello, P. Solinas, M. Di Ventra, F. Giazotto, Solitonic Josephson-based meminductive systems, *arXiv:1610.06807v1*, 2016.

[10]. E. T. Chen, J. T. Thornton, S.-H. Duh, P. T. Kissinger, Nanobiomimetic structured organo-metallic devices direct rapid real-time monitor atto molarity ATP in biological specimens, *TechConnect Briefs in Diagnostics*, 2019, pp. 423-426.

[11]. M. Ternes, M. Pivetta, F. Patthey, W.-D. Schneider, Creation, electronic properties, disorder, and melting of two-dimensional surface-state-mediated adatom, *Progress in Surface Science*, Vol. 85, Issue 1, 2010, pp. 1-27.

[12]. M. L. Bender, M. Komiyama, Cyclodextrin Chemistry, *Springer-Verlag*, Berlin, 1978.

[13]. J. Szejtli, Cyclodextrin and Their Inclusion Complexes, *Akademiai Kiado*, Budapest, 1982.

[14]. E. T. Chen, J. Thornton, Jr. C. Mulchi, Nanobiomimetic Memcapacitor Memory Devices Identify Circadian Rhythm Dysfunction and Predict Early Signs of "Epilepsy" Using Reentrant Energy-Sensory Images, *Advanced Manufacturing, Electronics and Microsystems: TechConnect Briefs*, 2015, pp. 200-203.

[15]. J. Thornton, Jr. C. Mulchi, P. T. Kissinger, E. T. Chen, Acetylcholine Repairs the Amyloid-beta Damage on Brain Circuitry and Memory Loss From a "Mutated Biomimetic Acetylcholinesterase" Neuronal Memcapacitor During Slow-Wave Sleeping, *Advanced Manufacturing, Electronics and Microsystems: TechConnect Briefs*, 2015, pp. 226-229.

[16]. E. T. Chen, J. Thornton, Jr. C. Mulchi, Early Forming a Hummingbird-like Hovering Neural Network Circuitry Pattern with Reentrant Spatiotemporal Energy-Sensory Orientation Privileged to Avoid "Epilepsy" Based on a Biomimetic Acetylcholinesterase Memcapacitor Prosthesis, *Sensors and Transducers Journal*, Vol. 191, Issue 8, 2015, pp. 84-99.

[17]. J. Thornton, Jr. C. Mulchi, P. T. Kissinger, E. T. Chen, In Vitro Restoration of an Amyloid-Beta Altered Network Circuitry in a 'Mutated Biomimetic Acetylcholinesterase' Memristor/Memcapacitor Neural Prosthesis, *Sensors and Transducers Journal*, Vol. 191, Issue 8, 2015, pp. 100-113.

[18]. B. Weiss, G. Ganepola, H. Freeman, Y. Hsu, M. Faupel, Surface Electrical Potentials as a New Modality in the Diagnosis of Breast Lesions-A Preliminary Report, *Breast Disease*, Vol. 7, Issue 2, 1994, pp. 91-98.

[19]. S. V. Sree, E. Ng, G. Kaw, R. Acharya U., B. Chong, The Use of Skin Surface Electropotentials for Breast Cancer Detection-Preliminary Clinical Trial Results Obtained Using the Biofield Diagnostic System, *J. of Medical Systems*, Vol. 35, Issue 1, 2011, pp. 79-86.

[20]. A. M. Hassan, M. Ei-Shenawee, Review of electromagnetic techniques for breast cancer detection, *IEEE Transactions in Magnetic*, online publisher, 2011.

[21]. A. M. Hassan, M. Ei-Shenawee, The Diffusion-Drift Algorithm for Modeling the Biopotential Signals of Breast Tumors, #TTT, *Cancer Detection and Diagnostics Technologies for Global Health Symposium at National Cancer Institute*, August 22-23, 2011.

[22]. L. Mitchell, N. A. Campbell, J. B. Reece, M. R. Taylor, Biology, 8th edition, *Pearson*, 2007.

[23]. S. L. Bonifacio, H. C. Glass, D. M. Ferriero, S. Peloquin, A new neurological focus in neonatal intensive care, *Nature Reviews Neurology*, Vol. 7, Issue 9, 2011, pp. 485-494.

[24]. E. T. Chen1, Y. Shen J. Thornton, C. Ngatchou1, S.-H. Duh, P. T. Kissinger, A Nanopore Biomimetic device quantitatively detects early-stage cancer cells; a Contour Map Multiple Variable Correlation Method assesses the heat of cancer cells released, *Techconnect Briefs, Nanotech*, Vol. 3, 2012, pp. 198-201.

[25]. E. T. Chen, J. Thornton, C. Ngatchou, S.-H. Duh, P. Kissinger, Nanostructured Biomimetic Memristor Sensors Used for Therapeutic Monitoring of The Brain Cancer, *NSTi-Nanotech*, Vol. 2, 2014, pp. 200-203.

[26]. E. T. Chen, Nanostructure Biomimetic Sensing and Energy Storage: Organic Memristor/Memcapacitors, in Dekker Encyclopedia of Nanoscience and Nanotechnology, *CRC Press*, 2014.

[27]. E. Chen, Nanostructured Biomimetic device for detecting a cancer cell or cancer cells, *US Patent No. 9,534,999*, January 3, 2017,

[28]. E. T. Chen, J. T. Thornton, P. T. Kissinger, S.-H. Duh, Utilization of the Flexible Fractional Josephson Toroidal Arrays for Sensing, Memory Storage, and Quantum Computing, *Sensors & Transducers*, Vol. 228, Issue 12, December 2018, pp. 30-47.

Published by International Frequency Sensor Association (IFSA) Publishing, S. L., 2019 (http://www.sensorsportal.com).